

Quantum pathways interference in nonadiabatic strong-field ionizations driven by elliptically polarized laser pulses

Yidian Tian(田亦电), Kunlong Liu(刘昆陇), and Yueming Zhou(周月明)

Citation: Chin. Phys. B, 2026, 35 (**4**): 043203. DOI: 10.1088/1674-1056/ae1c24
http://cpb.iphy.ac.cn; http://iopscience.iop.org/cpb

What follows is a list of articles you may be interested in

High-order harmonic generation of methane in an elliptically polarized field

Shu-Shan Zhou(周书山), Yu-Long Li(李玉龙), Zhi-Xue Zhao(赵志学), Man Xing(幸满), Nan Xu(许楠), Hao Wang(王浩), Jun Wang(王俊), Xi Zhao(赵曦), and Mu-Hong Hu(胡木宏)

Chin. Phys. B, 2025, 34 (**6**): 063202. DOI: 10.1088/1674-1056/adcb9d

Effect of orbital symmetry on atomic ionization in near-infrared laser fields

Manqi Xu(徐嫚琦), Shilin Hu(胡师林), Li Guo(郭丽), and Jing Chen(陈京)

Chin. Phys. B, 2025, 34 (**1**): 013202. DOI: 10.1088/1674-1056/ad8dbe

Manipulating the electron dynamics in the non-sequential double ionization process of Ar atoms by an orthogonal two-color laser field

Pengzhao Wang(王鹏昭), Lijie Qian(钱丽洁), Zhenrong Sun(孙真荣), and Yan Yang(杨岩)

Chin. Phys. B, 2024, 33 (**6**): 063201. DOI: 10.1088/1674-1056/ad2606

Attosecond ionization time delays in strong-field physics

Yongzhe Ma(马永哲), Hongcheng Ni(倪宏程), and Jian Wu(吴健)

Chin. Phys. B, 2024, 33 (**1**): 013201. DOI: 10.1088/1674-1056/ad0e5d

L-shell x-ray fluorescence relative intensities for elements with $62 \leq Z \leq 83$ at 18 keV and 23 keV by synchrotron radiation

M Alqadi, S AL-Humaidi, H Alkhateeb, and F Alzoubi

Chin. Phys. B, 2023, 32 (**8**): 083201. DOI: 10.1088/1674-1056/accb46

SPECIAL TOPIC — Ultrafast physics in atomic, molecular and optical systems

Quantum pathways interference in nonadiabatic strong-field ionizations driven by elliptically polarized laser pulses

Yidian Tian(田亦电)[1], Kunlong Liu(刘昆陇)[2,†], and Yueming Zhou(周月明)[1]

[1] *School of Physics and Wuhan National Laboratory for Optoelectronics, Huazhong University of Science and Technology, Wuhan* 430074, *China*
[2] *Great Bay Institute for Advanced Study, Dongguan* 523000, *China*

(Received 10 September 2025; revised manuscript received 30 October 2025; accepted manuscript online 6 November 2025)

Ultrafast phenomena initiated by strong-field ionization are commonly interpreted within classical or semiclassical frameworks based on electron trajectories. In this work, we theoretically investigate the energy-resolved photoelectron angular distributions in above-threshold ionization (ATI) induced by elliptically polarized ultraviolet (UV) pulses and unravel the underlying dynamics from the perspective of quantum-pathway interference. By numerically solving the three-dimensional time-dependent Schrödinger equation, we extract the contributions of the quantum pathways for an electron transitioning from the ground state to the continuum under pulses with different ellipticities. Our results demonstrate that for close-to-circularly polarized UV pulses, two quantum pathways govern the angular distribution for each ATI peak, and their interference produces a cosinusoidal oscillation in the photoelectron angular distributions, which is distinct from the Gaussian characteristic predicted by the traditional tunneling framework. In particular, the corresponding offset angle is shown to depend on the relative phase between these two dominant channels. As the ellipticity decreases, the increasing number of contributing pathways leads to a multiple-peak structure in the photoelectron angular distribution. The present study provides a quantum-mechanical perspective for understanding the angular streaking of nonadiabatic ionization in rotating fields.

Keywords: nonadiabatic strong-field ionization, elliptically polarized field, quantum pathways interference, angular offset

PACS: 32.80.Fb, 42.50.Hz, 33.80.Rv, 32.80.Rm

DOI: 10.1088/1674-1056/ae1c24 **CSTR:** 32038.14.CPB.ae1c24

1. Introduction

Strong-field ionization of atoms and molecules gives rise to a wealth of intriguing ultrafast phenomena, such as high-order harmonic generation,[1–4] frustrated tunneling ionization,[5–7] photoelectron holography[8–10] and Coulomb explosion.[11–13] There are two primary mechanisms in strong-field ionization.[14–16] One is tunneling ionization, in which the bound electron tunnels through the laser-distorted Coulomb barrier and becomes a free photoelectron. The other is multiphoton ionization, in which the electron gains sufficient energy from photon absorption to escape the binding potential. These two mechanisms coexist and compete in strong-field ionization.

The interaction of atoms and molecules with elliptically polarized strong laser fields has been extensively studied over the past few decades.[17–21] One of the most prominent applications of such fields is attosecond angular streaking, commonly known as the attoclock. This technique was initially proposed to investigate the timing of electron tunneling.[22–32] In this technique, the rotating electric field vector serves as the hand of a clock, mapping the time of ionization to the photoelectron emission angle. This elegant approach enables access to attosecond-scale timing information without requiring attosecond laser pulses. In addition, more findings indicate that the resulting photoelectron momentum distribution (PMD) contains a wealth of additional information beyond tunneling time.[33–38] The attoclock technique finds widespread application in the tunneling regime[22–41] which is often explained classically or semiclassically in terms of electron trajectories originating at a specific ionization time.

Recently, Trabert *et al.*[42] extended attoclock measurements to above-threshold ionization (ATI) with elliptically polarized (EP) ultraviolet (UV) pulses, revealing a counterintuitive energy-dependent angular offset trend that contradicts standard Coulomb-interaction predictions. Li *et al.*[43] and Xie *et al.*[44] further investigated the Coulomb effect in nonadiabatic tunneling. Their findings indicate that Coulomb-induced ionization time delay and Coulomb focusing lead to this nonintuitive trend. However, analyzing ionization mechanisms within an electron-trajectory framework in nonadiabatic ionization presents additional complexities. The Coulomb-distorted barrier loses its quasistatic character, and the rapidly rotating electric field introduces substantial complications to the electron trajectories. As demonstrated by Li *et al.*,[43] the

†Corresponding author. E-mail: liukunlong@gbu.edu.cn

© 2026 Chinese Physical Society and IOP Publishing Ltd. All rights, including for text and data mining, AI training, and similar technologies, are reserved.

emission angle no longer provides a one-to-one correspondence with the ionization time. This complexity makes it challenging to establish a comprehensive physical picture to interpret the mapping relation between the offset angle and the underlying physics. Furthermore, it is difficult to explain the observed cosinusoidal photoelectron angular distributions (PADs) by tracking electron trajectories in elliptically polarized pulse-induced nonadiabatic tunneling. To our knowledge, this observation has not been discussed in previous work.

In the present work, we develop a quantum-pathway interference framework to investigate the energy-resolved PADs in ionization induced by EP UV pulses. By numerically solving the three-dimensional time-dependent Schrödinger equation (3D-TDSE), we decompose the contributions of each partial wave to individual ATI rings. For near-circular polarization, we identify two dominant pathways that govern the angular distribution. Their interference produces cosinusoidal PADs, with the observed offset angle determined by their relative phase. In addition, we show that for pulses with small ellipticity, additional pathways emerge, producing multi-peak structures in the angular distributions.

2. Numerical methods

We numerically solve the 3D-TDSE to simulate the ionization dynamics of the H atom. In the velocity gauge, the propagation of the wave function is governed by (atomic units are used throughout unless otherwise stated)

$$\mathrm{i}\frac{\partial \Psi(\boldsymbol{r},t)}{\partial t} = \left(\frac{1}{2}\boldsymbol{p}^2 + \boldsymbol{A}(t)\cdot\boldsymbol{p} + V(\boldsymbol{r})\right)\Psi(\boldsymbol{r},t), \tag{1}$$

where $V(\boldsymbol{r}) = -1/\boldsymbol{r}$ is the Coulomb potential of the H atom (unless otherwise stated).

The ionization processes in the present work are induced by EP UV laser pulses. In the present work, we neglect the nondipole effect. Within the dipole approximation, the vector potential $\boldsymbol{A}(t)$ is defined as

$$\boldsymbol{A}(t) = \frac{1}{\omega}\frac{E_0}{\sqrt{\varepsilon^2+1}} f(t)(\sin(\omega t)e_y - \varepsilon\cos(\omega t)e_x), \tag{2}$$

where E_0 is the amplitude of the electric field. ω and ε denote the frequency and the ellipticity of the laser pulse, respectively. $f(t)$ is the envelope of the laser pulse defined as

$$f(t) = \sin^2\left(\frac{\pi t}{NT_0} + \frac{\pi}{2}\right), \tag{3}$$

where $N = 20$ is the number of optical cycles and T_0 is the optical period. All simulations use a laser pulse with a wavelength of 380 nm unless otherwise noted.

We propagate the time-dependent wave function $\Psi(\boldsymbol{r},t)$ in spherical coordinates. The wave function $\Psi(\boldsymbol{r},t)$ is expanded in spherical harmonics $Y(l,m)$ as

$$\Psi(\boldsymbol{r},t) = \sum_{l,m}\frac{R_{l,m}(r,t)}{r}Y(l,m), \tag{4}$$

where $R_{l,m}(r,t)$ is the radial component of the wave function, which is discretized using the finite-element discrete variable representation (FE-DVR) method.[45] The orbital angular momentum quantum number l and magnetic quantum number $|m|$ are chosen up to 30, and convergence has been ensured by varying the number of included partial waves. The time-dependent wave function $\Psi(\boldsymbol{r},t)$ is propagated using the split-Lanczos[46–49] method with the time step fixed at $\delta t = 0.01$ a.u. The maximum radial coordinate is chosen to be 1200 a.u., which is sufficiently large to contain the majority of the ionizing wave packets until the interaction process ends. The initial wave function is obtained by imaginary-time propagation and corresponds to the ground state of the H atom.

The ionization amplitude is obtained by projecting the final wave function onto the scattering states[46,49]

$$M(\boldsymbol{p}) = \langle\Psi_p(\boldsymbol{r})|\Psi(\boldsymbol{r},t_f)\rangle, \tag{5}$$

where $\Psi_p(\boldsymbol{r})$ is the normalized scattering state for the H atom. We have

$$M(\boldsymbol{p}) = \frac{1}{\sqrt{2\pi}p}\sum_{l,m}Y_{lm}(\hat{\boldsymbol{p}})f_{l,m}(\boldsymbol{p}), \tag{6}$$

where

$$f_{l,m}(\boldsymbol{p}) = (-\mathrm{i})^l\,\mathrm{e}^{-\mathrm{i}\sigma_l(\boldsymbol{p})}\int rR_{pl}(r)R_{lm}(r,t_f)\,\mathrm{d}r, \tag{7}$$

with $\sigma_l(\boldsymbol{p}) = \arg\Gamma(l+1-\mathrm{i}Z/p)$ being the Coulomb phase shift. Here $Z = 1$ is the nuclear charge for a hydrogenic system. The radial wave function $R_{pl}(r)$ is analytically given by

$$\begin{aligned} R_{pl}(r) = {} & \frac{2}{r}\frac{2^l\,\mathrm{e}^{\frac{\pi Z}{2p}}\left|\Gamma\left(l+1-\frac{\mathrm{i}Z}{p}\right)\right|}{(2l+1)!}\mathrm{e}^{-\mathrm{i}pr}(pr)^{l+1} \\ & \times {}_1F_1\left(l+1+\frac{\mathrm{i}Z}{p}, 2l+2, 2\mathrm{i}pr\right). \end{aligned} \tag{8}$$

where ${}_1F_1$ represents the confluent hypergeometric function.

The ionization amplitude $M(\boldsymbol{p})$ can be written as the sum of the contributions of each partial wave (see Eq. (6)). Thus, one can investigate the contribution of each partial wave to the ionization amplitude separately. The PMD is computed as

$$P(\boldsymbol{p}) = |M(\boldsymbol{p})|^2, \tag{9}$$

with intensities normalized to a maximum of 1 unless stated otherwise.

3. Results and discussion

An EP laser field can be analytically written as the superposition of two counter-rotating circularly polarized laser fields, as shown in Fig. 1

$$\boldsymbol{A}_{\rm EP}(t) = \boldsymbol{A}_{\rm L}(t) + \boldsymbol{A}_{\rm R}(t), \tag{10}$$

where $\boldsymbol{A}_{\rm L}(t)$ and $\boldsymbol{A}_{\rm R}(t)$ are the vector potentials of the left-handed circularly polarized (LCP) and right-handed circularly polarized (RCP) laser fields, respectively, which are given by

$$\boldsymbol{A}_{\rm L}(t) = \frac{1+\varepsilon}{2\omega}\frac{E_0}{\sqrt{\varepsilon^2+1}} f(t)(\sin(\omega t)\boldsymbol{e}_y - \cos(\omega t)\boldsymbol{e}_x), \tag{11}$$

$$\boldsymbol{A}_{\rm R}(t) = \frac{1-\varepsilon}{2\omega}\frac{E_0}{\sqrt{\varepsilon^2+1}} f(t)(\sin(\omega t)\boldsymbol{e}_y + \cos(\omega t)\boldsymbol{e}_x), \tag{12}$$

The electric dipole selection rules dictate that $\Delta L = \pm 1$ and $\Delta m = -1$ for LCP photon absorption, and $\Delta L = \pm 1$ and $\Delta m = +1$ for RCP photon absorption. Therefore, for EP laser-field-driven multiphoton ionization, the distinct pathways associated with LCP and RCP photon absorption give rise to interference in the PMD.

Figure 2 shows the calculated PMDs for different laser ellipticities obtained by numerically solving the TDSE. In all cases, the PMDs are anisotropic and exhibit oscillations in the angular direction. These oscillations are induced by the interference of different pathways. For near-circular polarization, each ATI ring displays a two-lobe structure, as shown in Figs. 2(a) and 2(b). As the ellipticity decreases, additional peaks emerge in the angular distributions, reflecting the increasing complexity of the interfering pathways.

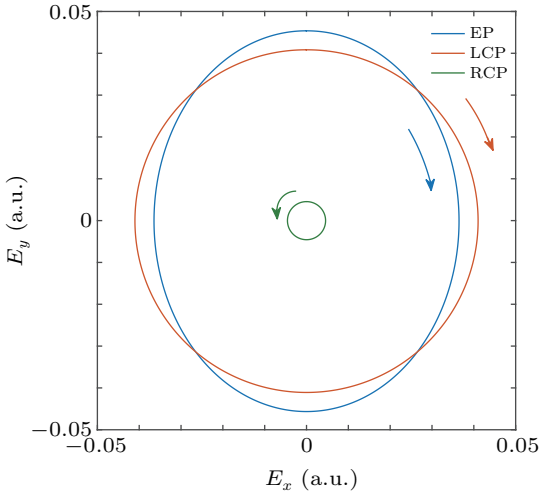


Fig. 1. The electric field of the elliptically polarized laser pulse and its corresponding left- and right-circularly polarized components. The electric field is calculated as $\boldsymbol{E}(t) = -\partial \boldsymbol{A}(t)/\partial t$. The laser intensity and ellipticity are 1.2×10^{14} W/cm^2 and 0.85, respectively.

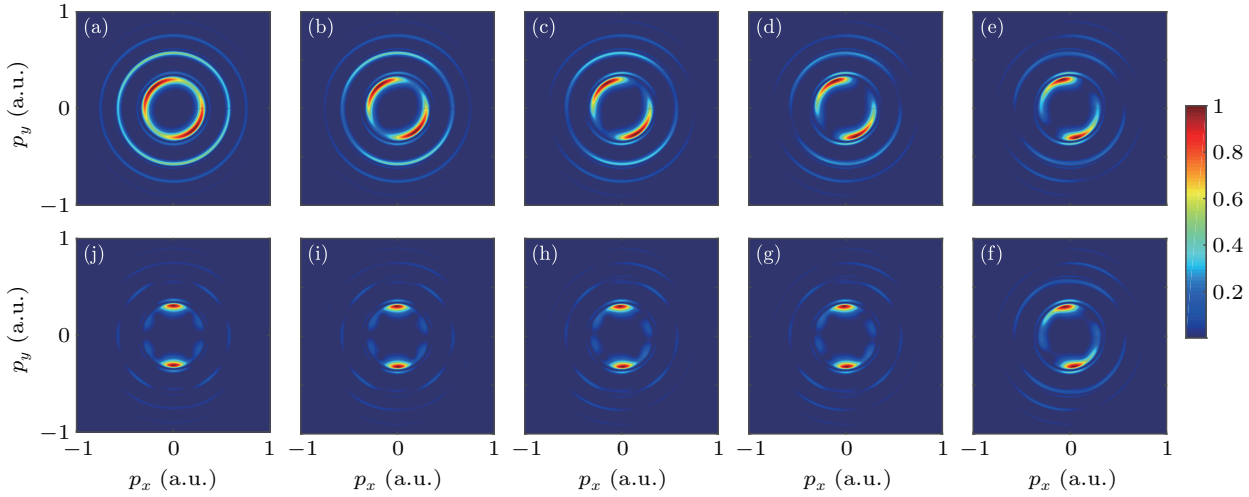


Fig. 2. The PMDs for the ionization of the H atom driven by EP laser pulses with different ellipticities: (a) $\varepsilon = 0.9$, (b) $\varepsilon = 0.8$, (c) $\varepsilon = 0.7$, (d) $\varepsilon = 0.6$, (e) $\varepsilon = 0.5$, (f) $\varepsilon = 0.4$, (g) $\varepsilon = 0.3$, (h) $\varepsilon = 0.2$, (i) $\varepsilon = 0.1$, and (j) $\varepsilon = 0$. The laser intensity is 1.2×10^{14} W/cm^2.

Here, we first discuss the ionization induced by close-to-circularly polarized laser fields. In this case, the amplitude of the LCP component is much greater than that of the RCP component $[(1+\varepsilon)/(1-\varepsilon) \gg 1]$. Thus, LCP photon absorption significantly outweighs RCP photon absorption. Figure 3 illustrates the two main channels for each ATI: (i) exclusive absorption of LCP photons, and (ii) absorption of one RCP photon with the remaining photons being LCP photons. These two channels generate photoelectron wave packets with the same energy but distinct angular momenta, giving rise to the observed oscillations.

To validate our theoretical analysis, we calculate the contributions of each partial wave to the PMDs. Figure 4(a) shows the PMD for ionization driven by a close-to-circular EP laser field. One can see three ATI peaks separated by the UV photon energy, which allows the investigation of each energy peak separately. Figures 4(b)–4(d) show the contributions of each partial wave to the three ATI peaks. Due to the selection rules, partial waves with odd parity dominate for ATI1 and ATI3, whereas partial waves with even parity dominate for ATI2. Moreover, one can see that the two main partial waves are $w_{5,-5}$ (partial wave $l = 5$ and $m = -5$) and $w_{3,-3}$ (partial

wave $l = 3$ and $m = -3$) for ATI1, $w_{6,-6}$ and $w_{4,-4}$ for ATI2, and $w_{7,-7}$ and $w_{5,-5}$ for ATI3. These two partial waves are produced by the two pathways illustrated in Fig. 3, providing strong confirmation of our physical picture.

Further verification comes from reproducing the angular-resolved spectra using only the two dominant partial waves, as shown in Fig. 5. The excellent agreement with the results obtained by considering all partial waves demonstrates that these two pathways indeed govern the ionization process induced by near-circular UV pulses.

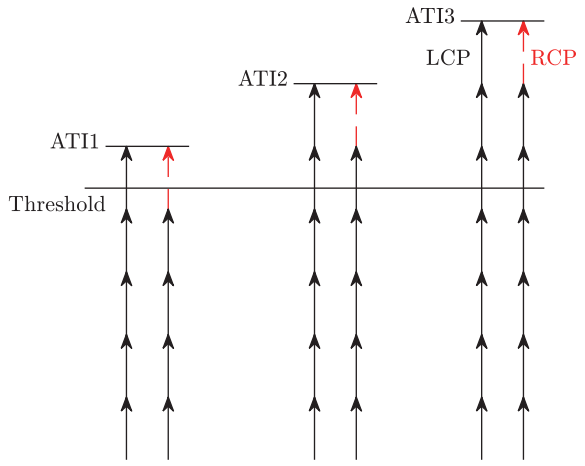


Fig. 3. Schematic energy diagram of the two main pathways illustrating the ionization of the H atom driven by a close-to-circular UV laser pulse for three ATI peaks.

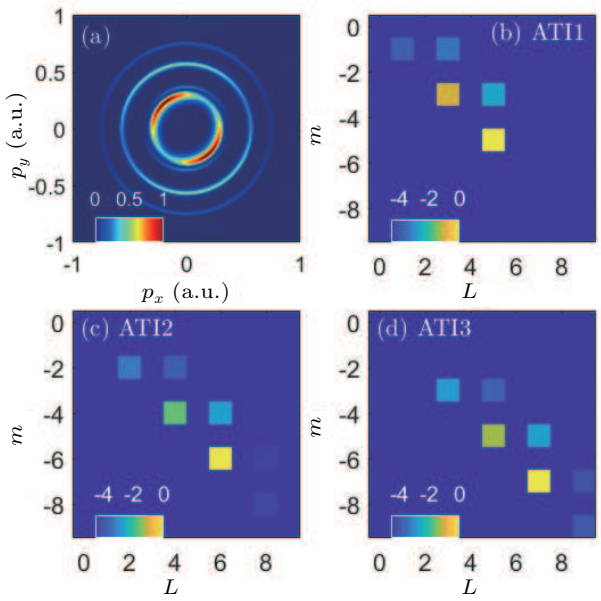


Fig. 4. (a) The PMDs for ionization driven by EP UV laser pulses. (b)–(d) The contributions of each partial wave to the three ATI peaks: (b) ATI1, (c) ATI2, and (d) ATI3. The laser ellipticity and intensity are 0.85 and 1.2×10^{14} W/cm^2, respectively. The data in (b)–(d) are shown on logarithmic scales.

To obtain more details, we investigate the location of the maximum of the angular distributions. Figure 6(a) shows the offset angle of each ATI peak as a function of laser ellipticity considering all partial waves (solid line) and considering the two dominant partial waves (dashed line). One can see that the offset angles remain nearly constant when only two partial waves are considered. In addition, the deviation between the complete and restricted partial-wave calculations gradually decreases and eventually becomes negligible as the laser ellipticity increases.

To understand these features, we analyze the ionization amplitude $M(\boldsymbol{p})$ in the laser polarization plane

$$M(p_r,\phi) = \sum_{l,m} A_{l,m}(p_r)\, \mathrm{e}^{(\mathrm{i}m\phi + \mathrm{i}\phi_{l,m})}, \tag{13}$$

where $A_{l,m}(p_r)$ is the amplitude independent of ϕ, and $\phi_{l,m}$ is the phase at the direction of the minor axis of the polarization ellipse ($\phi = 0$ in this work). In the case where only two dominant partial waves are considered, $M(\boldsymbol{p})$ can be written as

$$\begin{aligned} M_2(p_r,\phi) \;=\; & A_{n,-n}(p_r)\, \mathrm{e}^{(-\mathrm{i}n\phi + \mathrm{i}\phi_{n,-n})} \\ & + A_{n-2,-n+2}(p_r)\, \mathrm{e}^{[-\mathrm{i}(n-2)\phi + \mathrm{i}\phi_{n-2,-n+2}]}, \end{aligned} \tag{14}$$

where n represents the number of absorbed photons. $n = 5, 6, 7$ for ATI1, ATI2, and ATI3, respectively. Substituting Eq. (14) into Eq. (9), one can obtain

$$\begin{aligned} P_2(p_r,\phi) \;=\; & A^2_{n,-n}(p_r) + A^2_{n-2,-n+2}(p_r) \\ & + A_0 \cos\left(2\phi + \phi_{n,-n} - \phi_{n-2,-n+2}\right). \end{aligned} \tag{15}$$

This reveals that when only two dominant partial waves are considered, the angular distribution takes the theoretical form $A_0 \cos\left[2(\phi - \alpha_{\mathrm{off}})\right] + B_0$, where the offset angle α_{off} can be written as

$$\alpha_{\mathrm{off}} = \frac{\Delta\phi_n}{2}, \tag{16}$$

with $\Delta\phi_n = \phi_{n-2,-n+2} - \phi_{n,-n}$. As shown by the white dashed line in Fig. 5, the PADs resulting from the coherent summation of the two dominant pathways exhibit a clear cosinusoidal oscillation. Due to the involvement of other pathways, a minor deviation from this ideal form is observed in the complete partial-wave calculations. Furthermore, when only two partial waves are considered, the offset angle is determined by the relative phase between the two main pathways, as shown in Fig. 3. As expected, Fig. 6(b) demonstrates that the relative phases of the two channels remain constant with increasing ellipticity, consistent with the stable offset angles observed in Fig. 6(a).

To gain more insight into the trend of the offset angle, we calculate the relative yield of specific partial waves as a function of laser ellipticity, as shown in Fig. 7. One can see that with increasing laser ellipticity, the proportion of $w_{n,-n}$ increases, eventually approaching saturation. All other partial waves including $w_{n-2,-n+2}$ rapidly decrease as the laser ellipticity increases. This selective enhancement stems from the rapid decline of the RCP amplitude with increasing ellipticity

(see Eq. (12)), thereby preferentially suppressing pathways involving RCP photon absorption. Thus, the reduced deviation between the complete and restricted partial-wave calculations observed in Fig. 6(a) can be explained by the diminishing contributions from these other pathways.

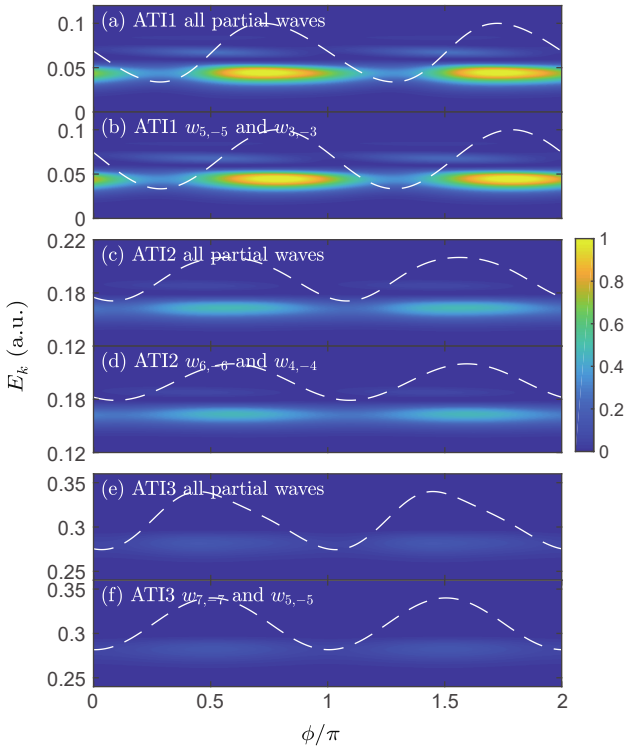


Fig. 5. The angular-resolved photoelectron energy spectra for each ATI peak [(a) and (b) ATI1, (c) and (d) ATI2, (e) and (f) ATI3] and the corresponding angular distributions (white dashed line). In (a), (c), and (e), all partial waves are considered. In (b), (d), and (f), only the two dominant partial waves are considered. The laser parameters are the same as in Fig. 4.

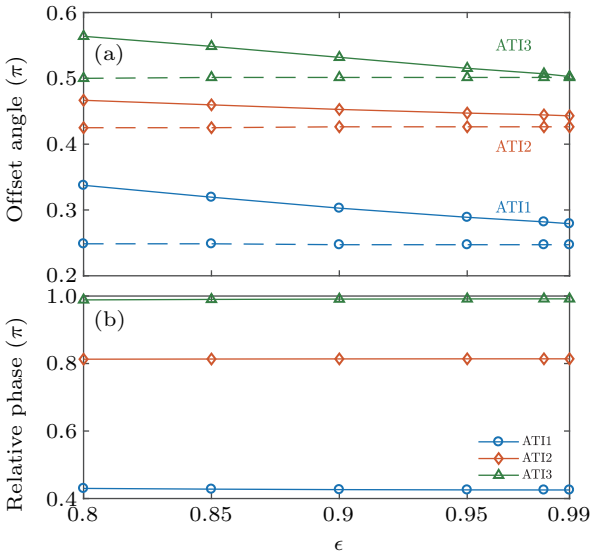


Fig. 6. (a) The offset angles of each ATI peak as a function of laser ellipticity, considering all partial waves (solid line) and only the two dominant partial waves (dashed line). The offset angle is defined as the most probable emission angle with respect to the minor axis of the laser polarization ellipse. (b) The relative phases of the two dominant partial waves as a function of laser ellipticity, defined as $\phi_{3,-3} - \phi_{5,-5}$ for ATI1, $\phi_{4,-4} - \phi_{6,-6}$ for ATI2, and $\phi_{5,-5} - \phi_{7,-7}$ for ATI3. Other laser parameters are the same as in Fig. 4.

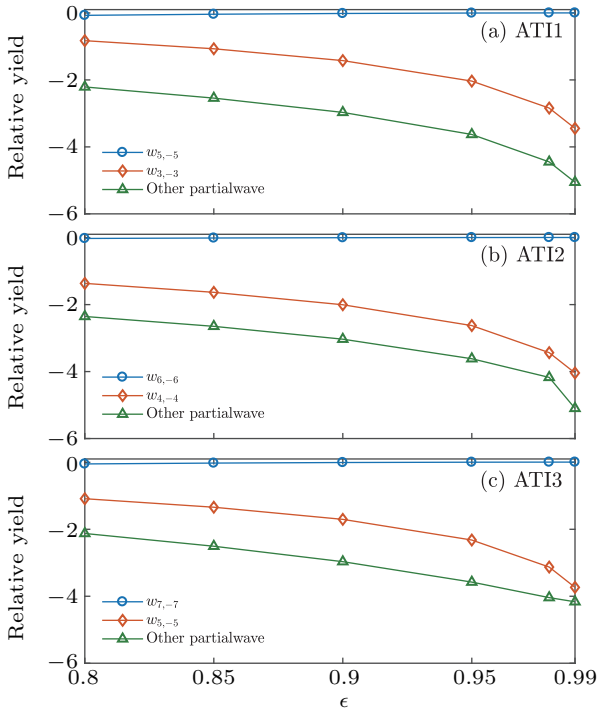


Fig. 7. The relative yields of specific partial waves with respect to the sum of all partial waves as a function of laser ellipticity. The data are shown on logarithmic scales. Other laser parameters are the same as in Fig. 4.

To further assess the robustness of our findings, we performed additional calculations at different laser intensities and wavelengths. As shown in Fig. 8, the two primary ionization channels remain dominant across a substantial range of these parameters. This confirms that our central result is not coincidental but is consistently observed under varied laser conditions.

It is recognized that nonadiabatic effects can impart a net linear momentum to electrons.[50] In our work, these effects primarily influence the relative phase between the two dominant quantum pathways, thereby modifying the resulting angular offset in the photoelectron distribution. Crucially, however, the nonadiabatic effect does not alter the fundamental dominance of these two channels. Therefore, the core findings of our work regarding the identified interference mechanism remain robust.

So far, our numerical calculations and theoretical analysis have shown that the absorption of zero or a single RCP photon constitutes the two dominant pathways in close-to-circular fields. With increasing laser ellipticity, the contributions of other channels further decrease. In addition, the corresponding angular distributions approximately follow the form $A_0 \cos[2(\phi - \alpha_{\text{off}})] + B_0$, which is distinct from the Gaussian distribution characteristic of the tunneling regime, and the location of the maximum is determined by the phase shift between the two dominant pathways.

Next, we turn to the ionizations in fields with smaller laser ellipticities. As shown in Fig. 9(a), for smaller laser ellipticity

fields, the PADs deviate from the form $A_0\cos[2(\phi-\alpha_{\rm off})]+B_0$. In the case $\varepsilon=0.6$, the distribution becomes asymmetric around the most probable emission angle. As the ellipticity decreases further, the PADs exhibit more peaks. This observation arises because the RCP and LCP amplitudes become comparable at small laser ellipticities, making pathways involving more than one RCP photon absorption non-negligible.

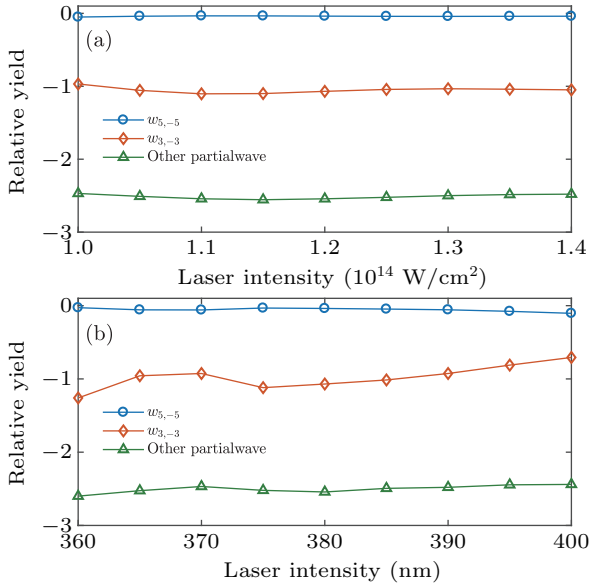


Fig. 8. The relative yields of specific partial waves of ATI1 with respect to the sum of all partial waves as a function of laser intensity (a) and wavelength (b). The data are shown on logarithmic scales. Other laser parameters are the same as in Fig. 4.

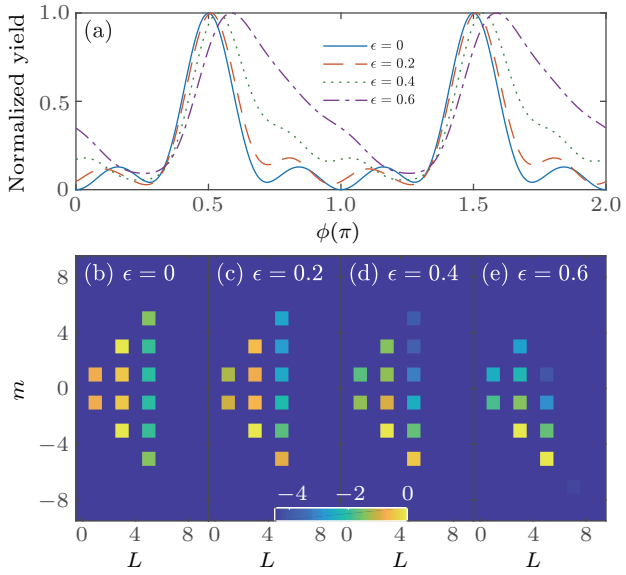


Fig. 9. (a) Normalized PADs for ATI1 at different laser ellipticities. (b)–(e) Contributions of each partial wave to ATI1 for different laser ellipticities: (b) $\varepsilon=0$, (c) $\varepsilon=0.2$, (d) $\varepsilon=0.4$, and (e) $\varepsilon=0.6$. The laser intensity is 1.2×10^{14} W/cm^2. The data in panels (b)–(e) are shown on logarithmic scales.

To gain more details, we analyze the contributions of individual partial waves. One can see that, in the case of $\varepsilon=0.6$, $w_{3,-3}$ and $w_{5,-5}$ remain the dominant partial waves, consistent with the observations in close-to-circular fields. With decreasing laser ellipticity and a corresponding increase in the probability of RCP photon absorption, the contributions of partial waves with higher m increase, while those with lower m decrease. In the linear polarization case ($\varepsilon=0$), a clear symmetry emerges between $m>0$ and $m<0$.

In these cases, one cannot consider only two partial waves. Here, the PMDs in the polarization plane are expressed as

$$P(p_r,\phi) = \sum_{l,m}A^2_{l,m}(p_r)+\sum_{l,m}\sum_{l',m'}A_{l,m}(p_r)A_{l',m'}(p_r) \times\cos[(m-m')\phi+\phi_{l,m}-\phi_{l',m'}]. \quad (17)$$

The frequency of the oscillation is determined by the term $\sum_{l,m}\sum_{l',m'}\cos[(m-m')\phi+\phi_{l,m}-\phi_{l',m'}]$. Consequently, in small ellipticity fields, frequency components other than 2ϕ become significant.

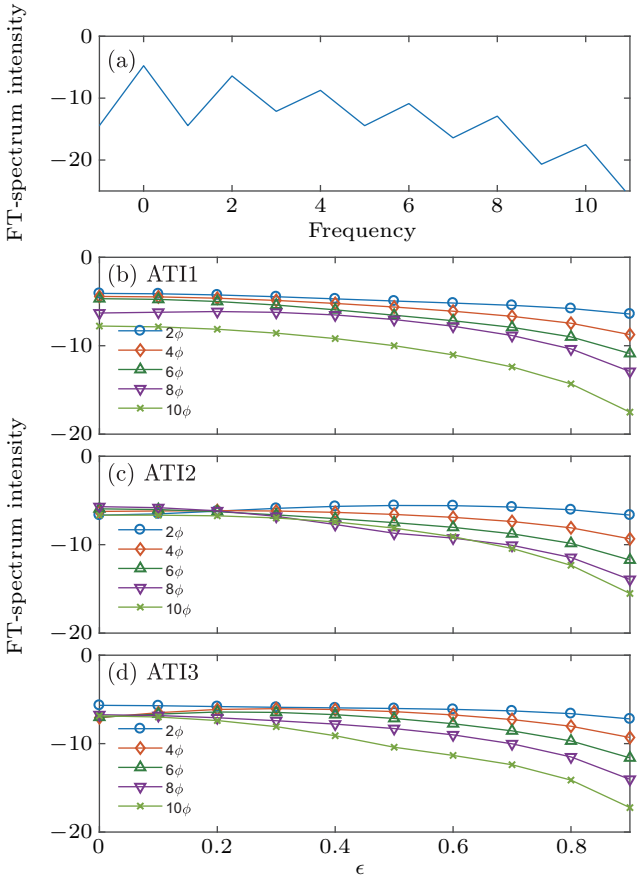


Fig. 10. (a) Fourier transform spectrum of the PAD for ATI1 with laser ellipticity $\varepsilon=0.9$. (b)–(d) Fourier transform spectrum intensities as a function of laser ellipticity for different frequency components: (b) ATI1, (c) ATI2, and (d) ATI3. The data are shown on logarithmic scales.

For a further investigation into the contributions of each frequency component, we apply the Fourier transform (FT) to the PADs, denoted as $\mathscr{F}(P(\phi))$, where the variable ϕ is the photoelectron emission angle. The result is shown in Fig. 10(a). One can see that the FT spectrum exhibits multiple peaks, each corresponding to a distinct frequency component. Figures 10(b)–10(d) show the ellipticity dependence of these frequency components for the three ATIs. In the case

of close-to-circular pulses, the 2ϕ-frequency component dominates for all three ATIs. With decreasing laser ellipticity, higher-frequency components increase rapidly. At small laser ellipticity, the higher-frequency components become comparable with the 2ϕ component, leading to the multi-peak structure observed in the PADs. In addition, compared to ATI1, higher-frequency components play a more significant role in ATI2 and ATI3. This trend arises because higher-order ATIs involve more complex pathways due to the increased number of absorbed photons.

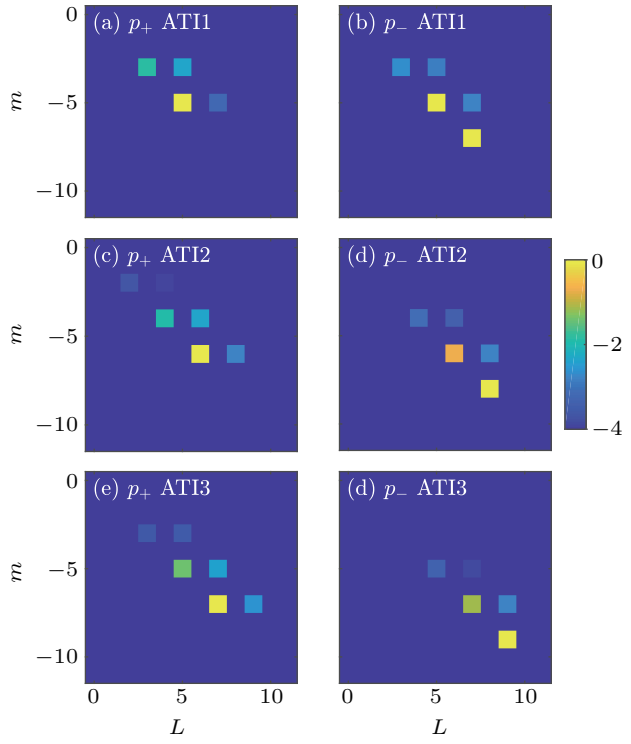


Fig. 11. The contributions of each partial wave to the three ATIs for initial states p_+ and p_-, respectively. The Coulomb interaction is defined as $V(r) = -(Z_c + a_1\exp(-a_2 r) + a_3 r\exp(-a_4 r) + a_5\exp(-a_6 r))/r$, with $Z_c = 1$, $a_1 = 16.039$, $a_2 = 2.007$, $a_3 = -25.543$, $a_4 = 4.525$, $a_5 = 0.961$, and $a_6 = 0.443$ for argon.[51] The laser parameters are the same as in Fig. 4. The data are shown on logarithmic scales.

To summarize, in small laser ellipticity fields, the pathways involving multiple RCP photon absorptions cannot be neglected. Their interference generates high-frequency oscillations, giving rise to the multi-peak structures in the PADs.

To further strengthen the generality of the present work, we perform calculations for argon (Ar), which features a p-state initial orbital. The results in Fig. 11 confirm that the two identified channels remain dominant across all three ATI orders for both the p_+ and p_- orbitals. In addition, a difference is observed in the angular momentum composition of the dominant partial waves between these orbitals, as a consequence of their different magnetic quantum numbers. This difference provides a potential scheme for producing spin-polarized electrons.[52–56]

4. Conclusion

In conclusion, we have established an analytical framework for investigating nonadiabatic ionizations induced by EP UV pulses. The numerical results and theoretical analysis show that the zero- or one-RCP-absorption channels are the two dominant pathways, which govern the angular distribution in close-to-circularly polarized fields and produce a cosinusoidal oscillation in the PADs. Our theoretical analysis reveals that the location of the maximum depends on the relative phase between these two channels. In addition, we have shown that in the case of small laser ellipticity, the increasing number of contributing pathways produces higher-frequency oscillation components, leading to the observed multi-peak structures. The present study provides a quantum-mechanical insight into nonadiabatic ionization in rotating fields and advances our understanding of nonadiabatic angular streaking.

Acknowledgments

This project is supported by the National Key Research and Development Program of China (Grant No. 2023YFA1406800), the National Natural Science Foundation of China (Grant Nos. 12174133, 11874163, and 12021004), and the Innovation Project of Optics Valley Laboratory (Grant No. OVL2021ZD001). The computing work in this paper is supported by the public computing service platform provided by the Network and Computing Center of HUST.

References

[1] Paul P M, Toma E S, Breger P, Mullot G, Augé F, Balcou Ph, Muller H G and Agostini P 2001 *Science* **292** 1689
[2] Sansone G, Benedetti E, Calegari F, Vozzi C, Avaldi L, Flammini R, Poletto L, Villoresi P, Altucci C, Velotta R, Stagira S, De Silvestri S and Nisoli M 2006 *Science* **314** 443
[3] Itatani J, Levesque J, Zeidler D, Niikura H, Pépin H, Kieffer J C, Corkum P B and Villeneuve D M 2004 *Nature* **432** 867
[4] Xiao F, Wang L, Bai G R, Zheng Z G, Sun X, Ji T F, Sun Y C, Wang J C, Wang X W and Zhao Z X 2025 *Chin. Phys. Lett.* **42** 043701
[5] Nubbemeyer T, Gorling K, Saenz A, Eichmann U and Sandner W 2008 *Phys. Rev. Lett.* **101** 233001
[6] von Veltheim A , Manschwetus B, Quan W, Borchers B, Steinmeyer G, Rottke H and Sandner W 2013 *Phys. Rev. Lett.* **110** 023001
[7] Yun H, Mun J H, Hwang S I, Park S B, Ivanov I A, Nam C H and Kim K T 2018 *Nat. Photonics* **12** 620
[8] Huismans Y, Rouzée A, Gijsbertsen A, *et al.* 2011 *Science* **331** 61
[9] Bian X B and Bandrauk A 2012 *Phys. Rev. Lett.* **108** 263003
[10] Meckel M, Staudte A, Patchkovskii S, Villeneuve D, Corkum P, Dorner R and Spanner M 2014 *Nat. Phys.* **10** 594
[11] Esry B S, Sayler A M, Wang P Q, Carnes K D and Ben-Itzhak I 2006 *Phys. Rev. Lett.* **97** 013003
[12] Madsen C B, Anis F, Madsen L B and Esry B D 2012 *Phys. Rev. Lett.* **109** 163003
[13] Guo K Y, Hu X Q, Li M, Jia C C, Zhang S B, Cao C P, Xie W X, Cao W, Liu K L, Zhou Y M, Wu Y, Wang J G and Lu P X 2024 *Ultrafast Sci.* **4** 1
[14] Yudin G L and Ivanov M Yu 2001 *Phys. Rev. A* **64** 013409
[15] Ivanov M Yu, Spanner M and Smirnova O 2005 *J. Mod. Opt.* **52** 165
[16] Ma Y Z, Ni H C and Wu J 2024 *Chin. Phys. B* **33** 013201
[17] Liu Y P, Xie W H, Li M, Cao C P, Zhou Y M and Lu P X 2023 *J. Phys. B: At. Mol. Opt. Phys.* **56** 105601

[18] Odenweller M, Takemoto N, Vredenborg A, Cole K, Pahl K, Titze J, Schmidt L Ph H, Jahnke T, Dörner R and Becker A 2011 *Phys. Rev. Lett.* **107** 143004

[19] He P L, Takamoto N and He F 2015 *Phys. Rev. A* **91** 063413

[20] Xie H, Li M, Luo S Q, Li Y, Zhou Y M, Cao W and Lu P X 2017 *Phys. Rev. A* **96** 063421

[21] Mao X D, Liu K L, Ni H C and Wu J 2025 *Phys. Rev. A* **111** 033113

[22] Eckle P, Pfeiffer A N, Cirelli C, Staudte A, Dörner R, Muller H G, Büttiker M and Keller U 2008 *Science* **322** 1525

[23] Eckle P, Smolarski M, Schlup P, Biegert J, Staudte A, Schöffler M, Muller H G, Dörner R and Keller U 2008 *Nat. Phys.* **4** 565

[24] Pfeiffer A N, Cirelli C, Smolarski M, Dimitrovski D, Abu-samha M, Madsen L B and Keller U 2012 *Nat. Phys.* **8** 76

[25] Torlina L, Morales F, Kaushal J, Ivanov I, Kheifets A, Zielinski A, Scrinzi A, Muller H G, Sukiasyan S, Ivanov M and Smirnova O 2015 *Nat. Phys.* **11** 503

[26] Zimmermann T, Mishra S, Doran B R, Gordon D F and Landsman A S 2016 *Phys. Rev. Lett.* **116** 233603

[27] Ni H C, Saalmann U and Rost J M 2016 *Phys. Rev. Lett.* **117** 023002

[28] Camus N, Yakaboylu E, Fechner L, Klaiber M, Laux M, Mi Y, Hatsagortsyan K Z, Pfeifer T, Keitel C H and Moshammer R 2017 *Phys. Rev. Lett.* **119** 023201

[29] Bray A W, Eckart S and Kheifets A S 2018 *Phys. Rev. Lett.* **121** 123201

[30] Orunesajo E, Abubakar S, Oguh B, Ranathunga Y, Dubois J, Rico L, Taíeb R, Lee S K and Li W 2025 *Phys. Rev. Lett.* **134** 203201

[31] Yu M, Liu K, Li M, Yan J Q, Cao C P, Tan J, Liang J T, Guo K Y, Cao W, Lan P F, Zhang Q B, Zhou Y M and Lu P X 2022 *Light Sci. Appl.* **11** 215

[32] Douguet N and Bartschat K 2022 *Phys. Rev. A* **106** 053112

[33] Boge R, Cirelli C, Landsman A S, Heuser S, Ludwig A, Maurer J, Weger M, Gallmann L and Keller U 2013 *Phys. Rev. Lett.* **111** 103003

[34] Liu K L, Luo S Q, Li M, Li Y, Feng Y D, Du B J, Zhou Y M, Lu P X and Barth I 2019 *Phys. Rev. Lett.* **122** 053202

[35] Liu K L and Barth I 2017 *Phys. Rev. Lett.* **119** 243204

[36] Bloch E, Larroque S, Rozen S, Beaulieu S, Comby A, Beauvarlet S, Descamps D, Fabre B, Petit S, Taíeb R, Uzan A J, Blanchet V, Dudovich N, Pons B and Mairesse Y 2021 *Phys. Rev. X* **11** 041056

[37] Fehre K, Eckart S, Kunitski M, Janke C, Trabert D, Rist J, Weller M, Hartung A, Pitzer M, Schmidt L Ph H, Jahnke T, Dörner R and Schöffler M S 2019 *Phys. Rev. Res.* **1** 033045

[38] Hofmann M, Trabert D, Geyer A, Jahnke T, Kunitski M, Anders N, Kruse J, Rist J, Schmidt L Ph H, Schöffler M S, Eckart S and Dörner R 2024 *Phys. Rev. Res.* **6** 043176

[39] Ni H C, Brennecke S, Gao X, He P L, Donsa S, Brezinová I, He F, Wu J, Lein M, Tong X M and Burgdorfer J 2020 *Phys. Rev. Lett.* **125** 073202

[40] Tian Y D, Liu K L, Wang Y C, Zhou Y M and Lu P X 2024 *J. Chem. Phys.* **160** 114311

[41] Zhao Q, Peng Y G, Che J J, Chen C, Wang S, Xin G G and Chen Y J 2025 *Chin. Phys. B* **34** 093201

[42] Trabert D, Anders N, Brennecke S, Schöffler M S, Jahnke T, Schmidt L Ph H, Kunitski M, Lein M, Dörner R and Eckart S 2021 *Phys. Rev. Lett.* **127** 273201

[43] Li X K, Liu X W, Wang C C, Ben S, Zhou S P, Yang Y Z, Song X H, Chen J, Yang W F and Ding D J 2024 *Light Sci. Appl.* **13** 250

[44] Xie W H, Li Z C, Li M, Liu Y P, Liu Y, Cao C P, Guo K Y, Liu K L, Zhou Y M and Lu P X 2024 *Phys. Rev. Lett.* **133** 183201

[45] Rescigno T N and McCurdy C W 2000 *Phys. Rev. A* **62** 032706

[46] Jiang W C and Tian X Q 2017 *Opt. Express* **25** 26832

[47] Liang J T, Zhou Y M, Jiang W C, Yu M, Li M and Lu P X 2022 *Phys. Rev. A* **105** 043112

[48] Liu M Q, Wang X Q, Jia L J, Yan P G and Jiang W C 2023 *Phys. Rev. A* **108** 013102

[49] Ke Q H, Zhou Y M, Liao Y J, Liang J T, Zhao Y, Tan J, Li M and Lu P X 2021 *Front. Phys.* **16** 52503

[50] Mao X D, Ni H C and Wu J 2025 *Phys. Rev. A* **110** 063113

[51] Tong X M and Lin C D 2005 *J. Phys. B: At. Mol. Opt. Phys.* **38** 2593

[52] Barth I and Smirnova O 2013 *Phys. Rev. A* **88** 013401

[53] Hartung A, Morales F, Kunitski M, Henrichs K, Laucke A, Richter M, Jahnke T, Kalinin A, Schöffler M, Schmidt L Ph H, Ivanov M, Smirnova O and Dörner R 2016 *Nat. Photonics* **10** 526

[54] Liu K L, Renziehausen C, Rost J and Barth I 2018 *Phys. Rev. Lett.* **121** 203201

[55] Hu Y B, Ma Q F, Liu K L, Tian Y D, Li M, Zhou Y M and Lu P X 2023 *Phys. Rev. A* **107** 033108

[56] He P L, Zhang Z H, Hatsagortsyan K Z and Keitel H C 2025 *Phys. Rev. Lett.* **134** 163201